Temperature dependence of a Raman CO_2 densimeter from 23 to 200°C and 7.2 to 248.7 MPa: Evaluation of density underestimation by laser heating

Yuuki Hagiwara [1,*], Tetsuma Kawano [1], Kohei Takahata [1], Junji Torimoto [2] and Junji Yamamoto [3]

[1] Graduate School of Science, Hokkaido University, Kita 10 Nishi 8, Kita-ku, Sapporo, Hokkaido 060-0810

[2] Ore Genesis Research Unit, Project Team for Development of New-Generation Research Protocol for Submarine Resources, JAMSTEC, 2-15, Natsushimacho, Yokosuka-shi, Kanagawa, 237-0061, Japan

[3] The Hokkaido University Museum, Kita 10 Nishi 8, Kita-ku, Sapporo, Hokkaido 060-0810

* Corresponding author: Yuuki Hagiwara

e-mail: hagi@eis.hokudai.ac.jp

Tel.: +81-11-706-4733

Abstract

Unintended local temperature enhancement by excitation laser might change Raman spectral features and potentially lead to misinterpretation of the data. To evaluate robustness of Raman CO_2 densimeters in the presence of laser heating, we investigate the relation between temperature (T, °C), density (ρ, g/cm^3), and Fermi diad split (Δ, cm^{-1}) using a high-pressure optical cell at 23–200°C and 7.2–248.7 MPa. Results indicate that Δ decreases concomitantly with increasing temperature for a constant density in all density regions investigated. This result suggests that the density estimated based on Δ might be underestimated if the fluid is heated locally by the laser. Combining results of earlier studies with those of the present study indicates that the temperature dependence of Δ ($|(\partial\Delta/\partial T)_\rho|$) has a maximum value around 0.6–0.7 g/cm^3. Consequently, at very high densities such as 1.1–1.2 g/cm^3, $|(\partial\Delta/\partial T)_\rho|$ is small. Thus, Δ at such densities is less affected by laser heating. However, at densities below approximately 0.7 g/cm^3, although $|(\partial\Delta/\partial T)_\rho|$ becomes smaller at lower densities, the relative density decrease becomes larger even for a small density decrease because the density itself becomes smaller. Therefore, at such densities, a density decrease of more than 10% was observed for some fluid inclusions, even at typical laser powers for inclusion analysis. Finally, to accurately estimate the density even in the presence of laser heating, we show that it is

effective to estimate the intercept Δ from the correlation between Δ and laser power, and substitute it into Δ–ρ relations.

Keywords

Carbon dioxide, Densimeter, Fermi resonance, Fluid inclusions, Laser heating

1. INTRODUCTION

Fluid inclusions with compositions approximated as CO_2-rich systems are common in many geologic environments, including hydrothermal ore deposits,[1–3] medium-grade to high-grade metamorphic rocks,[1,4–7] and mantle xenoliths[1,8,9]. In many geological settings, the density of those fluid inclusions has been studied to track volcanic plumbing systems,[10–13] to ascertain the depth provenance of mantle xenoliths,[14–18] and to identify the pre-eruptive volatile contents of magmas[19–24]. Although microthermometry is the principal method for estimating the density of CO_2-rich inclusions, this method is effective only when inclusion is sufficiently large to measure the CO_2 homogenization temperature accurately because change in the fluid phase is determined using an optical microscope. This size limitation is generally approximately 5 μm.[25] Furthermore, if the host mineral has a large absorption coefficient of visible light, then measuring the homogenization temperature might be difficult, even for inclusions larger than 5 μm. Additionally, because the accuracy decreases at low and extremely high densities, microthermometry is applicable only when the density of CO_2 inclusions is 0.65–1.18 g/cm^3.[26]

Raman spectroscopy is used as an alternative or complementary technique to estimate CO_2 fluid density when estimating fluid density by microthermometry is

60 difficult. The method is applicable to a wide density range of 0.001–1.24 g/cm^3 and to
61 small inclusions down to sub-micrometer size and to inclusions in colored minerals,
62 where the homogenization temperature is difficult to measure, as long as Raman
63 scattering photons with a sufficient number for quantitative analysis reach the detector.[27–
64 29] Raman-based CO_2 densimetry uses the relation between CO_2 fluid density (ρ) and
65 Fermi diad splitting ($\Delta = \nu^{+}_{\mathrm{F.D.}} - \nu^{-}_{\mathrm{F.D.}}$).[18,25,27–42] Although Raman CO_2 densimeter is
66 useful, some caution is necessary for application of this method to density
67 measurements of natural fluid inclusions: 1) Effect of intermolecular interactions
68 between CO_2 and trace molecules other than CO_2 on the spectral properties of CO_2,[28,32–
69 37,43–46] 2) discrepancy in the Δ–ρ relations derived in earlier studies,[27,37,47] and 3)
70 apparent density reduction because of the local temperature rise caused by excitation
71 lasers[48]. Regarding the first problem, this method has been improved vigorously to
72 quantify the fluid pressure in inclusions with various P–V–T–x properties. Its
73 applicability is now expanding to include the CO_2±N_2±CH_4 [28,34,36,45,46,49] and CO_2–
74 H_2O±NaCl systems[28,32,35,37,44]. The second difficulty can be resolved by adding a
75 correction term δ to the measured Δ. This correction term can be found by optimizing
76 the residual sum of squares between the density estimated by any Δ–ρ relation from the
77 Δ values of several standard fluid inclusions and the known density to the minimum.[37]

Alternatively, in the region where the Δ–ρ relation can be approximated linearly, it is also effective to derive an original Δ–ρ relation applicable to the Raman system to be used, using two standard fluid inclusions with known density.[27] For the third one, because $(\partial\Delta/\partial T)_\rho$ is always negative, at least in the density range investigated by earlier studies,[35,36] the density estimated from the measured Δ might be underestimated if the excitation laser causes unintended heating. Nevertheless, few examples exist to verify the conditions and the extent to which it affects the measurement accuracy.[48]

To assess the uncertainty that laser heating imposes on density estimation, one must ascertain the amount of change in Δ when the temperature of a fluid inclusion with a certain density ρ is increased unintentionally by T°C because of laser heating, i.e., $|(\partial\Delta/\partial T)_\rho|$. The value of $|(\partial\Delta/\partial T)_\rho|$ can be obtained directly from the Δ–ρ–T relation. Several attempts have been undertaken to characterize high P–T CO_2 Raman spectra.[28,35,36,42,44,50] The temperature dependence of Δ at a given density ($|(\partial\Delta/\partial T)_\rho|$) below 0.7 g/cm^3 was found to be smaller for lower densities.[35,36] However, regarding the density dependence of $|(\partial\Delta/\partial T)_\rho|$ at > 0.7 g/cm^3, several studies have yielded somewhat different conclusions.[28,35,36] According to the Δ–ρ–T relation for pure CO_2 derived by Wang et al.[35] using a high-pressure optical cell (HPOC), $|(\partial\Delta/\partial T)_\rho|$ becomes smaller at higher densities, greater than 0.7 g/cm^3. However, when using the relation

96 derived by Sublett et al.[36], $|(\partial\Delta/\partial T)_\rho|$ becomes larger at higher densities above 0.7 g/cm^3,
97 which is inconsistent with results reported by Wang et al.[35]. Therefore, some
98 disagreement exists with results of earlier studies of density dependence of $|(\partial\Delta/\partial T)_\rho|$
99 conducted at densities higher than 0.7 g/cm^3.

100 The density dependence of $|(\partial\Delta/\partial T)_\rho|$ is consistent at low densities but
101 inconsistent at high densities in earlier studies perhaps because few data have been
102 reported for earlier studies undertaken in conditions above ambient temperature and at
103 densities higher than 1.0 g/cm^3 (Figure 1). For this study, we extended the pressure
104 range of investigation markedly beyond that of earlier studies. We examined the Δ–ρ–
105 T relation at 23–200°C and 7.2–248.7 MPa using a HPOC filled with pure CO_2 having
106 density of 0.694–1.203 g/cm^3. Based on the results, we acquired calibration curves to
107 estimate density at various temperatures. Then we compared the curves with those
108 obtained from published data. Finally, to elucidate how the fluid density and physical
109 properties of the host minerals affect the amount of fluid density underestimation by
110 laser heating in the analysis of fluid inclusions, the value of Δ of CO_2-rich fluid
111 inclusions with various densities in Cr-spinel and orthopyroxene was measured at
112 various laser powers. The goals of this study are 1) to clarify the discrepancy between
113 previous studies on the density dependence of $|(\partial\Delta/\partial T)_\rho|$ at high densities, 2) to show

114 the extent to which laser heating introduces uncertainties in the density estimation of
115 natural fluid inclusions depending on the host mineral species and fluid density, and 3)
116 to propose an analytical procedure to accurately estimate the density even in the
117 presence of laser heating.
118
119 **2. EXPERIMENTAL**
120 **2.1 High-pressure and high-temperature optical cell**
121 We used a high-temperature and high-pressure cell (PC-400 ms; Syn Corp.) to
122 investigate the temperature-dependence of Δ–ρ relations. The high-pressure cell can
123 create a fluid with respective maximum pressure and temperature of 400 MPa and
124 200°C, but because the pressure resistance of the high-pressure generator is 200 MPa,
125 the uppermost pressure is limited by the pressure resistance of the high-pressure
126 generator. To measure the fluid at higher pressure than the resistance of the high-
127 pressure generator, high-pressure fluid was generated using two pressurization methods.
128 One is isothermal compression, by which pressure is applied with a hydraulic jack while
129 maintaining the cell temperature constant. Using this method, measurements were
130 performed from 23°C to 200°C in approximately 20°C increments under 10 temperature
131 conditions. Under the experimental conditions, CO_2 was single-phase. In addition,

spectra were acquired up to 153.8 MPa under each temperature condition. We pressurized the CO_2 fluid gradually while maintaining the temperature constant. Furthermore, we measured the Raman spectra twice under each *P–T* condition. The *P–T* conditions measured using this method are shown by filled red squares on *P–T* projection of the CO_2 phase diagram calculated according to the explanation by Pitzer and Sterner[51] EOS (Figure 1). Regarding the other method, the pressure was increased at first to 153.8 MPa while maintaining the high-pressure cell at a low temperature (approx. −10°C) using a cryogen. Subsequently, we closed valve-1 (shown in Figure 2) between the cell and the high-pressure generator. We raised the cell temperature to the target. Using the latter method, we were able to generate fluid with pressures of 153.5–248.7 MPa, which is higher than the pressure resistance of the high-pressure generator. Using this method, after reaching the target temperature, the Raman spectrum was measured while gradually reducing the pressure by loosening valve-1 (Figure 2). The measurements were repeated more than three times at each *P–T* condition. The measurements are taken at temperatures from 60°C to 200°C in 20°C increments under eight temperature conditions. The *P–T* conditions measured using the latter method are shown by the open blue squares in Figure 1 together with *P–T* conditions measured in earlier studies using HPOC and fused silica capillary capsules (FSCC).[28,31,33–36,50]

150 Detailed *P–T* measurement conditions are presented in Tables S1 and S2. Hereinafter,
151 we designate the former and latter experiments respectively as “isothermal
152 pressurization experiments” and “near isochoric heating experiments.”

153 Figure 2 is a schematic drawing of the HPOC and its attached components. To
154 remove air from the high-pressure system, the high-pressure line was flushed with CO_2
155 (99.99% purity; Sun Chemical Corp.) for about 30 s before pressurizing the fluid. The
156 temperature was measured using a K-type thermocouple placed in direct contact with
157 the fluid. The fluid temperature during analysis of isothermal pressurization
158 experiments and near isochoric heating experiments were, respectively, kept to
159 uncertainty below ± 0.1°C and ± 0.5°C through PID control of the cartridge heater
160 (Tables S1 and S2). The room temperature was 22.1–23.6°C throughout the analysis.
161 We measured pressures using a PG-2TH digital pressure transducer with a manometer
162 (WGA-650A; Kyowa Electronic Instruments Co., Ltd.). The overall accuracy of the
163 pressure transducer was ± 0.2% of the reading. The accuracy compensation temperature
164 of the pressure gauge was −10 to 70°C. The pressure changes during analyses of
165 isothermal pressurization experiments and near isochoric heating experiments were,
166 respectively, less than ± 0.1 MPa and ± 1.1 MPa. In the case of the near isochoric heating
167 experiments, the pressure change during the analysis was large because of the large

168 pressure difference between the high-pressure cell and generator.

169

170 **2.2 Measurement of Raman spectra of CO_2 in a HPOC at constant laser power**

171 Raman spectra of the CO_2 fluid were obtained using a micro-Raman spectrum
172 analysis system set up at the Hokkaido University Museum. Raman spectra were
173 acquired during excitation by a diode-pumped solid-state laser (532 nm, Gem 532;
174 Laser Quantum), and were acquired using a spectrometer with 75 cm focal length
175 (Acton SP-2750; Princeton Instruments, Inc.) and a CCD camera (1650 × 200 pixels,
176 16 μm width, iVac; Andor Technology). A 50-μm core diameter multimode fiber served
177 as the pinhole for confocality and as the entrance slit to the spectrometer. The laser
178 power (P_{ill}) was 13.2 mW at the sapphire window surface. The excitation laser was
179 focused through a super long working distance 10× objective (T Plan SLWD; Nikon
180 Corp.; N.A. = 0.2). The wavenumber dispersion for each pixel of the present Raman
181 system when using a grating of 1800 lines/mm was 0.28 cm^{-1}/pixel at 1400 cm^{-1}. The
182 accuracy in identification of peak position was enhanced further by application of a
183 curve-fitting technique.[52] Earlier studies demonstrated that least-squares fitting
184 improves precision by approx. 30 times compared to the value based on the detector
185 pixel resolution.[52,53] Each CO_2 band was fitted to a Gaussian and Lorentzian mixing

curve. Spectra were collected in a single window ranging from 1007.53 to 1485.58 cm^{-1}, which covers the main peaks of the Fermi diad of CO_2 and two well-established reference peaks of neon occurring at 1221.73 and 1449.19 cm^{-1}. Data were collected using two accumulations of 50 s or 100 s.

This study did not specifically examine the absolute value of the peak position, but instead emphasized investigation of the difference in the peak position of Fermi diad, which is not susceptible to the nonlinearity of the optical system. Nevertheless, to reduce mechanical errors in the optical system induced by changes in the measurement environment, the measured values were corrected using the atomic emission spectrum of the Ne lamp fixed to the optical system. Although Lamadrid et al.[27] calibrated Δ using the two Ne lines appearing at 1031 and 1458 cm^{-1} surrounding the Fermi diad, the Δ was calibrated using the following equation because the wavelengths of the excitation lasers used for this study differ from the wavelengths used for theirs.

$$\Delta_{\text{Ne calib}} = \Delta^{\text{raw}} \times \left(\frac{227.46}{\Delta_{\text{mes}}^{\text{Ne}}} \right) \quad (1)$$

In that equation, $\Delta_{\text{Ne calib}}$ denotes the corrected splitting of the Fermi diad, $\Delta_{\text{mes}}^{\text{Ne}}$ represents the measured separation between 1449.19 and 1221.73 cm^{-1} Ne emission lines. Δ^{raw} stands for the measured splitting of Δ in the CO_2 Raman spectrum. Tables S1 and S2 show the wavenumber difference of corrected Δ ($\Delta_{\text{Ne calib}}$) together with the *P–T*

203 conditions of the fluid.

204

205 **2.3 Measurement of CO_2 Raman spectra as a function of laser power**

206 **2.3.1 HPOC experiments**

207 To assess the temperature-dependence of Δ–ρ relations accurately, the local
208 heating caused by the focused laser must also be considered because it might affect the
209 Raman spectrum in a similar fashion to that by which the cartridge heater heats the
210 HPOC and the fluids.

211 The temperature measurement can be performed using two peaks with much
212 lower intensity next to the Fermi diad (1264.8 and 1409.0 cm^{-1}; $v^{-}_{H.B.}$ and $v^{+}_{H.B.}$),
213 designated as hot bands.[54] Hot bands putatively arise from transitions that originate from
214 excited vibrational states that are higher in energy than the ground vibrational state and
215 which are attributable to the thermal energy of the molecules. The hot bands are also
216 attributable to Fermi resonance between $v_1 + v_2$ and $3v_2$.[55] Earlier studies have assessed
217 CO_2 hot band availability for use as a thermometer.[25,48,56–58] These thermometers use the
218 hot band to Fermi diad intensity ratio ($[I^{+}_{H.B.}+I^{-}_{H.B.}]/[I^{+}_{F.D.}+I^{-}_{F.D.}]$). Peak heights of $v^{+}_{F.D.}$,
219 $v^{-}_{F.D.}$, $v^{+}_{H.B.}$, and $v^{-}_{H.B.}$ are represented respectively as $I^{+}_{F.D.}$, $I^{-}_{F.D.}$, $I^{+}_{H.B.}$, and $I^{-}_{H.B.}$. In the
220 studied P–T region, temperature enhancement of about >4°C can be detected using a

221 hot-band thermometer.[58] Therefore, to investigate the influence of the local laser
222 heating, we monitored the change of Δ and hot band to Fermi diad intensity ratio while
223 changing P_{ill} at two pressure conditions: 7.2 and 153.8 MPa.

224 We measured Δ and the hot band to Fermi diad intensity ratio using the same
225 10× objective (T Plan SLWD, N.A. = 0.2; Nikon Corp.) and excitation laser (532 nm) as
226 those used for the HPOC experiments. Measurements were made while changing P_{ill} at
227 the sample surface from 1.7 to 16.7 mW. The P_{ill} during the experiments were measured
228 using a laser power meter (PD300-ROHS; Ophir Optronics Ltd.). The uncertainty of the
229 measured P_{ill} was ±3%. The fluid pressures were 7.2 MPa and 153.8 MPa at 23°C,
230 respectively corresponding to 0.783 g/cm^3 and 1.204 g/cm^3. The spectrum was
231 measured five times at each P_{ill}. Table 1 presents the results.

232

233 **2.3.2 Natural fluid inclusions**

234 We selected a total of seven CO_2-rich fluid inclusions hosted in mineral separates
235 of orthopyroxene and Cr-spinel, which are derived from a mantle xenolith designated as
236 "En2A" from Ennokentiev, Sikhote-Alin, Far Eastern Russia. Petrological descriptions
237 were presented by Yamamoto et al.[15]. The fluid inclusion compositions were
238 investigated using Raman spectroscopic analysis. Volatile species other than CO_2 are

not detected from the seven inclusions. Although no H_2O liquid phase was visible under microscopic observation, trace amounts of H_2O might be wetting the wall of inclusions.[6,59] For the fluid inclusions in orthopyroxene, the partial homogenization temperatures of the carbonate phase to liquid were measured using a heating–cooling stage (THMS600; Linkam Scientific Instruments Ltd.) at Hokkaido University. Homogenization temperature was not reported for Cr-spinel because of its high absorption coefficient, which made observation of the phase transition difficult, but the density estimated from the measured Δ value is presented in Table 2. The instrument was calibrated using the melting points of H_2O (0.0 °C) in synthetic pure H_2O fluid inclusions. Homogenization was recorded at the heating rate of 0.1 °C/min. Fluid densities are calculated as described by Span and Wagner[60].

The individual inclusions were measured in the order of 4.7, 11.6, 7.9, and 14.4 mW using almost identical Raman apparatus to that described section 2.2. The only difference from the configuration explained above is the objective lens: a 50× objective lens (LU Plan, N.A. = 0.8; Nikon Corp.) was used. The sample was placed on a glass slide. During the measurement, room temperature was maintained at 20.5±1.0°C. Considering that the temperature increases of inclusions per unit laser power in Cr-spinel and orthopyroxene were, respectively, approx. 6°C/mW and approx. 1°C/mW,[48] this

257 variation in room temperature is sufficiently smaller than the expected temperature
258 increases of inclusions during analysis. Given the same temperature increase of inclusions
259 per unit of laser power, the CO_2-rich phase of all inclusions is homogenized into a single
260 supercritical fluid, liquid, or gas phase during the analysis. Measurements were taken five
261 times at each P_{ill}. Table 2 presents the average Δ value of five measurements and their
262 standard deviation (1σ) at each P_{ill}. The duration of every Raman analysis is three
263 accumulations of 100 s for inclusion in Cr-spinel and two accumulations of 100 s for
264 those in orthopyroxene. This is because, in the case of Cr-spinel, both incident laser and
265 Raman scattering light are more absorbed by the host mineral because of its high
266 absorption coefficient, resulting in a low number of CO_2 Raman scattering photons
267 detected per unit time.

268 The measured Δ (Δ^{raw}) values are first calibrated using measured and known
269 distances between the Ne lines according to the explanation presented by Lamadrid et
270 al.[27] ($\Delta_{Ne\ calib}$ in Table S3). Subsequently, discrepancies in the calibration curves between
271 laboratories were corrected by adding the correction term $\delta_{Eq.2}$ to $\Delta_{Ne\ calib}$. Finally,
272 corrected Δ (Δ_{calib}) are defined as $\Delta_{calib} = \Delta_{Ne\ calib} + \delta_{Eq.2}$. According to Hagiwara et al.[37],
273 $\delta_{Eq.2}$ was calculated using Equation (2), Equation (10) of Hagiwara et al.[37], and the 2 Δ_{Ne}
274 $_{calib}$ obtained from the standard fluid inclusions with known density (0.786 and 1.167

275 g/cm^3). Using the correction procedures described above, the differences between known
276 density of standard fluid inclusions and density calculated by substituting Δ_{calib} into
277 Equation (2) were found to be less than 0.2%. The values of $\delta_{Eq.2}$ are shown in the footnote
278 of Table S3.
279
280 **3. RESULTS**
281 **3.1 Temperature-dependence of Δ–*ρ* relations**
282 We investigated the *P*–*T* dependence of Δ at temperatures of 23–200°C and
283 pressures of 7.2–248.7 MPa using HPOC. In this study, the density corresponding to the
284 *P*–*T* conditions of every analysis was calculated using the method described by Span
285 and Wagner[60] EOS for CO_2. In all, total of 151 Δ values obtained from 23 to 200°C are
286 portrayed in Figure 3a. In agreement with results reported from earlier studies, all Δ
287 values shift systematically to higher values with increasing density at constant
288 temperature.[18,25,27–32,34–36,42] In addition, the $(\partial\rho/\partial\Delta)_T$ rates obtained from our data
289 decrease gradually with increasing density, especially at high density. This tendency
290 was also observed from earlier studies conducted at high density (Figure 3b).[29,31,37,42]
291 The $(\partial\Delta/\partial T)_\rho$ rate was found to be negative in all density regions studied, from 0.7 to
292 1.2 g/cm^3, which is consistent with results obtained from earlier studies for 0.0 to 1.0

293 g/cm^3 [28,34–36,50].

294 The main findings obtained from HPOC experiments are that the temperature
295 derivative of Δ at constant density ($(\partial\Delta/\partial T)_\rho$) depends strongly on the density and that
296 the $(\partial\Delta/\partial T)_\rho$ rates are always negative, even at high density (Figure 3a). Although the
297 temperature dependence of the Δ–ρ relations exists throughout the entire density range
298 that was analyzed (0.7–1.2 g/cm^3), $|(\partial\Delta/\partial T)_\rho|$ rates are maximum at approx. 0.7 g/cm^3;
299 they decrease as density increases from 0.7 g/cm^3 (Figure 4c).

300

301 **3.2 Regression analysis and error analysis**

302 The respective *P*–*T* changes during analysis of the isothermal pressurization
303 experiments were less than ± 0.1 MPa and ± 0.1°C. The *P*–*T* condition shown in Table
304 S2 is an average value obtained during analysis of the near isochoric heating
305 experiments. The *P*–*T* variation during the analysis was less than ± 1.1 MPa and ± 0.5°C
306 (Table S2). Density uncertainty caused by *P*–*T* fluctuation during Raman analysis was
307 lower than ± 0.0028 g/cm^3 (Tables S1 and S2). Measurements of 153.8 MPa at 120, 140,
308 160, and 180°C were taken in both the isothermal pressurization experiments
309 (increasing pressure cycle) and near isochoric heating experiments (decreasing pressure
310 cycle) to evaluate the effects of differences in the pressurization method. The

311 differences of Δ of the four pairs were −0.018, −0.029, +0.029, and +0.024 cm^{-1},
312 respectively, at 120, 140, 160, and 180°C. No systematic error resulted from the
313 difference in the pressure generation method.

314 To estimate the fluid density from the sample temperature and measured Δ, we
315 conducted regression analysis. The density of CO_2 fluid inclusions at elevated
316 temperatures can be found using the following polynomial equation.

$$\rho = a + bT^2 + cT^3 + d\Delta + e\Delta^2 + f\Delta^3 + g\Delta T + h\Delta^2 T + i\Delta T^2 + j\exp(\Delta) \quad (2)$$

317 Therein, *a* through *j* represent fitting parameters. These parameters and associated errors
318 are given in Table 3. In that equation, ρ (g/cm^3), T (°C), and Δ (cm^{-1}), respectively
319 represent the fluid density, temperature, and Fermi diad splits of CO_2. It is noteworthy
320 that "*T*" is not included in the explanatory variables in Equation (2) because we selected
321 them so that the *p*-values of all explanatory variables are less than 0.05. Instead, exp(Δ)
322 was added as an explanatory variable, which is particularly useful in reflecting the
323 characteristic that $(\partial\rho/\partial\Delta)_T$ becomes smaller at higher densities. Because the *p*-values of
324 all explanatory variables are less than 0.008, they are influential factors for the objective
325 variable. Equation (2) has a coefficient of determination (R^2) of 0.999. Equation (2) is
326 valid in the experimentally calibrated regime of 23°C ≤ T ≤ 200°C and 0.7 $g/cm^3 \leq \rho \leq$
327 1.2 g/cm^3 (Figure 1). The half of the difference between the upper and lower bounds of

the prediction interval at 1σ of the Equation (2) was lower than ± 0.0057 g/cm^3. Finally, the uncertainty in the density estimation based on Equation (2), which takes into account both the uncertainty in the model and the density variation during the analysis, is ± $\sqrt{0.0028^2+0.0057^2} \approx 0.006$ g/cm^3.

3.3 Laser heating effects during HPOC experiments

Absorption of excitation laser light by the optical window of the HPOC or CO_2 fluid itself might cause unintentional local temperature enhancement. In that case, Δ can be expected to decrease concomitantly with increasing P_{ill} because Δ decreases concomitantly with increasing temperature at constant density (Figure 3). However, all Δ values are within the range of error (Figures 5a and 5b). No systematic decrease was observed to occur along with the increase of P_{ill} (Figures 5a and 5b). Similarly, hot bands to the Fermi diad intensity ratio can increase with P_{ill} because it increases concomitantly with increasing temperature at constant density.[25,48,56–58] Although a temperature change of about > 4°C can be detected from the hot bands to the Fermi diad intensity ratio, the intensity ratio does not change systematically with P_{ill} (Figures 5c and 5d).[58] Therefore, results demonstrate that the influence of laser heating is lower than 4°C, at least under the present analytical conditions. Nevertheless, to avoid

346 possible heating effects, measurements are taken at the sample surface with P_{ill} of 13.2
347 mW. Therefore, the maximum laser heating during the HPOC experiment, if any, is
348 about 3°C (approx. $4\times\frac{13.2}{16.7}$°C). This temperature enhancement is sufficiently lower than
349 the experimental temperature range of 23–200°C. Therefore, we can ignore laser
350 heating effects in the HPOC experiments.
351
352 **3.4 Laser heating effects during natural fluid inclusion analysis**
353 Because Δ decreases monotonically with laser power (Table 2), the intercept of
354 the linear fitting between Δ_{calib} and P_{ill} ($\Delta_{intercept}$) can be regarded as Δ without laser
355 heating. For estimating the best fit straight line to data, we applied bivariate least-squares
356 fitting method (York method) using OriginPro9.0 software (OriginLab Corporation,
357 Northampton, US). Figure 6 presents the relation between "$\Delta_{intercept}-\Delta_{calib}$" and laser
358 power. For all fluid inclusions, Δ tends to decrease with laser power. The slope of the
359 relation between Δ and laser power $(\partial\Delta/\partial P_{ill})_\rho$ is, invariably, significant and negative
360 (Table 2). Details underlying the reason for this negative slope are explained in Section
361 4.2, but it is not attributable to the monotonic drift of the Raman system because the
362 measurements were performed in the order of 4.7, 11.9, 7.9, and 14.4 mW without
363 monotonically increasing (or decreasing) P_{ill}.

Figure 6a presents data for fluid inclusions with densities of 1.201, 0.919, 0.737, and 0.377 g/cm^3 in Cr-spinel. For inclusions with density higher than 0.7 g/cm^3, densities are calculated by substituting $\Delta_{intercept}$ into Equation (2). For inclusions with density lower than 0.7 g/cm^3, Δ_{calib} was defined as $\Delta_{Ne\ calib} + \delta_{Kawakami03}$, where $\delta_{Kawakami03}$ was calculated from the Δ–ρ relation of Kawakami et al.[42], Equation (10) of Hagiwara et al.[37], and Δ_{calib} for two standard fluid inclusions (Table S3). Then, the density was calculated by substituting $\Delta_{intercept}$ into the Δ–ρ relation presented by Kawakami et al.[42]. For the three inclusions with densities greater than 0.7 g/cm^3, $|(\partial\Delta/\partial P_{ill})_\rho|$ is shown to become smaller for higher densities (Figure 6a). A similar trend was obtained for fluid inclusions with densities of 1.167, 0.914, and 0.704 g/cm^3 in orthopyroxene. However, the $|(\partial\Delta/\partial P_{ill})_\rho|$ of fluid inclusions with density of 0.377 g/cm^3 in Cr-spinel is 0.0075±0.0033 cm^{-1}/mW, which is clearly lower than that of 0.737 g/cm^3 (0.0143±0.0020 cm^{-1}/mW). This is consistent with results of earlier studies, which show that below approx. 0.7 g/cm^3, $|(\partial\Delta/\partial T)_\rho|$ becomes a smaller value at lower densities. [35,36]

4. DISCUSSION

4.1 Effects of density on $\partial\Delta/\partial T$: Comparison with results of earlier studies

Many earlier studies have clarified details of the temperature dependence of

382 the relation between Δ and density.[28,31,32,34–36,42,44,50] To raise the accuracy of discussion
383 related to the temperature dependence of Δ, the differences of measurement conditions
384 among earlier studies such as spectral resolution, pressure measurement accuracy,
385 temperature range, and fluid composition must be clarified. After reviewing earlier
386 studies, we eventually chose to compare the results reported by Sublett et al.[36], Wang
387 et al.[35], and Wang et al.[28] with those of the present study. Details of the process of
388 selecting the earlier studies to be used for comparison with this study are presented in
389 Supporting Information.

390 Earlier studies have examined the density dependence of $|(\partial\Delta/\partial T)_\rho|$. Reports
391 have described that $|(\partial\Delta/\partial T)_\rho|$ becomes smaller at lower densities (Figure S1).[35,36] By
392 contrast, regarding density dependence of $|(\partial\Delta/\partial T)_\rho|$ at > 0.7 g/cm^3, several studies have
393 yielded somewhat different conclusions.[28,35,36] According to the Δ–T–ρ relation for
394 pure CO_2 derived by Wang et al.[35] using HPOC, $|(\partial\Delta/\partial T)_\rho|$ becomes smaller at densities
395 higher than 0.7 g/cm^3 (Figure 4a). This is supported by the fact that their data obtained
396 using FSCC shows that $|(\partial\Delta/\partial T)_\rho|$ is larger at 0.743 g/cm^3 than at 0.807 g/cm^3. However,
397 using the relation derived by Sublett et al.[36], $|(\partial\Delta/\partial T)_\rho|$ becomes larger at densities
398 higher than 0.7 g/cm^3, which is inconsistent with the results reported by Wang et al.[35]
399 (Figure 4b). Furthermore, Wang et al.[28] investigated the temperature dependence of Δ

400 at 35–200°C and 40–200°C, respectively using natural and synthetic fluid inclusions in
401 quartz with densities of 0.7074 and 0.4676 g/cm^3. Results respectively portray that Δ
402 decreased concomitantly with increasing temperature up to 200°C by 0.19 cm^{-1} and 0.24
403 cm^{-1} (Figure 4a). Comparing the results obtained from the two fluid inclusions by Wang
404 et al.[28], there appears to be little density dependence of $|(\partial\Delta/\partial T)_\rho|$. Therefore,
405 disagreement exists between earlier studies of the density dependence of $|(\partial\Delta/\partial T)_\rho|$ at
406 densities higher than 0.7 g/cm^3.

407 Our results demonstrate that $|(\partial\Delta/\partial T)_\rho|$ decreases concomitantly with increasing
408 density for densities higher than 0.7 g/cm^3 (Figure 4c), which is consistent with results
409 reported by Wang et al.[35]. Our results support the results reported by Wang et al.[35]
410 more than those of Sublett et al.[36], probably because Wang et al.[35] obtained more data
411 at high densities than Sublett et al.[36] did. Therefore, this study, which specifically
412 examined high-density data, yielded results that are rather consistent with those reported
413 by Wang et al.[35] for densities higher than 0.7 g/cm^3. The fluid inclusions of Wang et
414 al.[28] at 0.7074 and 0.4676 g/cm^3 had similar $|(\partial\Delta/\partial T)_\rho|$, perhaps because the density
415 was 0.7074–0.4676 g/cm^3 at which the sign of $d|(\partial\Delta/\partial T)_\rho|/d\rho$ is reversed. Consequently,
416 the two fluid inclusions used by Wang et al.[28] might have coincidentally had densities
417 for which $|(\partial\Delta/\partial T)_\rho|$ is comparable mutually. Strictly speaking, however, the effect of

418 the amount of H_2O in the CO_2-rich inclusions should also be considered, as described
419 by Wang et al.[35], but because the amount of H_2O is unknown, we do not discuss it
420 further.

421 In summary, the combination of our Δ–T–ρ relation in the high-density region
422 and that in the low-density region investigated in results of earlier studies suggests that
423 density at which the sign of $\partial|(\partial\Delta/\partial T)_\rho|/\partial\rho$ is reversed exists around 0.6–0.7 g/cm^3.
424 Therefore, when the density of CO_2 fluid inclusions is measured using a Raman CO_2
425 densimeter, fluid inclusions with densities of approximately 0.6–0.7 g/cm^3 are the most
426 susceptible to Δ change because of laser heating.

427

428 **4.2 Apparent density reduction caused by laser heating**

429 **4.2.1 Causes of variation in $(\partial\Delta/\partial P_{\mathrm{ill}})_\rho$**

430 The values of Δ obtained from the fluid inclusions clearly decrease
431 concomitantly with increasing P_{ill}. The decrease shows density dependence (Figure 6).
432 These features can be explained well by the Δ–T–ρ relation (i.e., $(\partial\Delta/\partial T)_\rho$ is always
433 negative and $|(\partial\Delta/\partial T)_\rho|$ reaches its maximum at 0.6–0.7 g/cm^3) and the monotonic
434 temperature increase of the inclusion with increasing P_{ill}, but other factors that can
435 engender variations in $(\partial\Delta/\partial P_{\mathrm{ill}})_\rho$ must also be examined carefully.

Another mechanism that causes a reduction in Δ with increasing P_{ill} is the difference in the temperature increase of individual inclusions during analysis. In other words, the inclusions with density of 0.737 g/cm^3 of Cr-spinel and 0.704 g/cm^3 of orthopyroxene have the highest $|(\partial\Delta/\partial P_{ill})_\rho|$ in their respective host minerals, probably because those inclusions were the hottest during analysis. Because Hagiwara et al.[48] have demonstrated that the size and depth from the sample surface of the selected inclusions have little effect on laser heating, they will be excluded as factors in the difference in the magnitude of $|(\partial\Delta/\partial P_{ill})_\rho|$. Regarding size effect, the minimum and maximum inclusion radius in orthopyroxene are 4.9 μm and 9.3 μm, respectively, and the ratio of the laser heating coefficient ($B_{9.3\mu m}/B_{4.9\mu m}$) calculated by Figure 6b of Hagiwara et al.[48] is 0.95. Therefore, the difference in temperature increase due to the inclusion size difference is only 5%. The maximum temperature rise expected for inclusions in orthopyroxene is about 1°C/mW × 15 mW = 15°C, thus the temperature difference at that time is 15 × 0.05 = 0.75°C, and the change in Δ caused by this slight temperature difference would be negligible. In fact, no systematic correlation exists between the size and depth of inclusions and $|(\partial\Delta/\partial P_{ill})_\rho|$ (Tables 2 and S3). Furthermore, according to earlier studies, the temperature increase per unit of laser power in the same host mineral is almost identical for different inclusions.[48] Therefore, the difference in heating rates can be

454 excluded as a reason for the difference in $|(\partial\Delta/\partial P_{\mathrm{ill}})_\rho|$ between inclusions.

455 If one assumes that the temperature increase per unit laser power is nearly
456 constant for inclusions in the same host mineral, then $|(\partial\Delta/\partial T)_\rho| = |(\partial\Delta/\partial P_{\mathrm{ill}})_\rho|/(dT/dP_{\mathrm{ill}})$
457 $\propto |(\partial\Delta/\partial P_{\mathrm{ill}})_\rho|$. Therefore, similarly to the density dependence of $|(\partial\Delta/\partial T)_\rho|$ predicted by
458 the HPOC experiment, $|(\partial\Delta/\partial P_{\mathrm{ill}})_\rho|$ also can be expected to have a maximum value of
459 around 0.6–0.7 g/cm^3, and $|(\partial\Delta/\partial P_{\mathrm{ill}})_\rho|$ can be expected to decrease as the density
460 increases at >0.7 g/cm^3. In fact, inclusions with densities closest to 0.6–0.7 g/cm^3 have
461 the largest $|(\partial\Delta/\partial P_{\mathrm{ill}})_\rho|$ in each host mineral. In addition, for inclusions in both
462 orthopyroxene and Cr-spinel, for densities higher than 0.7 g/cm^3, the higher the density,
463 the smaller the $|(\partial\Delta/\partial P_{\mathrm{ill}})_\rho|$, which is consistent with the trend expected from HPOC
464 experiments. Therefore, one can infer that the combination of laser heating and the
465 temperature dependence of the Δ–ρ relations is responsible for the observed features of
466 $|(\partial\Delta/\partial P_{\mathrm{ill}})_\rho|$, such as $(\partial\Delta/\partial P_{\mathrm{ill}})_\rho$ always being negative and $|(\partial\Delta/\partial P_{\mathrm{ill}})_\rho|$ being largest for
467 inclusions with densities closest to 0.6–0.7 g/cm^3.

468

469 **4.2.2 Accurate density estimation in the presence of laser heating**

470 As expected from the results of HPOC experiments, the greatest decrease in Δ
471 for fluid inclusions in the 0–14.4 mW range was observed for the fluid inclusions in Cr-

472 spinel with density closest to 0.6–0.7 g/cm^3. For this inclusion (spinel03 fi146), the
473 density estimated by substituting the Δ_{calib} measured at 14.4 mW without considering
474 the effects of laser heating into Equation (2) is 0.655 g/cm^3, whereas the density
475 obtained by substituting the $\Delta_{intercept}$ corrected for the effect of laser heating into
476 Equation (2) is 0.737 g/cm^3. In this case, the density is underestimated by 0.082 g/cm^3
477 (approx. 12%). In addition, for the fluid inclusion of 0.373 g/cm^3 (spinel03 fi154),
478 where $|(\partial\Delta/\partial P_{ill})_\rho|$ is smaller than that of the inclusion of 0.737 g/cm^3, the decrease in
479 density itself is 0.052 g/cm^3, which is smaller than that of the inclusion of 0.737 g/cm^3.
480 However, in percent notation, the density underestimation is 15%, which is severer than
481 that of 0.737 g/cm^3. Therefore, even though $|(\partial\Delta/\partial P_{ill})_\rho|$ is small at densities lower than
482 0.6–0.7g/cm^3, the relative underestimation of density because of laser heating might be
483 rather more severe than for inclusions at 0.6–0.7g/cm^3. Therefore, for inclusions in host
484 minerals such as Cr-spinel, which have a large absorption coefficient and which are
485 affected strongly by laser heating, the density might be underestimated by about >10%,
486 even at typical laser power of 15 mW. For such inclusions, some correction is necessary
487 to estimate the density accurately. Underestimation of the density of fluid inclusions in
488 orthopyroxene (0.704 g/cm^3, opx06 fi005), which has almost identical density to that of
489 spinel03 fi146, is 3.4% according to the calculation presented above, which is one-

490 fourth that of Cr-spinel. The reason for this difference in density underestimation might
491 be that the temperature increase of the inclusions in Cr-spinel is greater than that in
492 orthopyroxene because the absorption coefficient of Cr-spinel (approx. 20 cm^{-1})[61] is
493 larger than that of orthopyroxene (approx. 9 cm^{-1})[62]. For an inclusion with density of
494 1.201 g/cm^3 in Cr-spinel, the underestimation is only 0.9% (= 0.010 g/cm^3) under the
495 conditions described above. Therefore, for densities of approx. 1.1–1.2 g/cm^3, where
496 $|(\partial\Delta/\partial T)_\rho|$ is small, the underestimation of density because of laser heating is small, even
497 in host minerals that are extremely sensitive to laser heating, such as Cr-spinel.
498 Therefore, at such very high densities, the effect of laser heating can be neglected in
499 many cases.

500 The following is an explanation of how to estimate the density accurately even
501 in the presence of laser heating, based on data of opx06 fi005, which had the largest
502 $|(\partial\Delta/\partial P_{ill})_\rho|$ among inclusions with known density. The densities obtained by
503 substituting Δ_{calib} into Equation (2) without correcting for the effect of laser heating
504 ($\rho_{\Delta_{calib}}$) are 0.699 ± 0.005 g/cm^3 at 4.7 mW, 0.692 ± 0.003 g/cm^3 at 7.9 mW, 0.682 ±
505 0.005 g/cm^3 at 11.9 mW, and 0.681 ± 0.003 g/cm^3 at 14.4 mW, respectively, which
506 become lower than the known density of 0.704 g/cm^3 as the laser power increases (Table
507 2). In the case of inclusions in orthopyroxene, at laser powers below 4.7 mW, the

508 deviation between ρ_{T_h} and $\rho_{\Delta_{calib}}$ is less than 0.005 g/cm^3 (= 0.7%). The effect of laser
509 heating on density estimation is almost equivalent to the density uncertainty in the
510 calibration curve itself. Thereby, the effect of laser heating can be ignored. However, at
511 14.4 mW, the deviation between ρ_{T_h} and $\rho_{\Delta_{calib}}$ is 0.023 g/cm^3 (= 3.4%), which is
512 clearly an underestimation of the true value. In this way, when the effect of heating
513 cannot be neglected, substituting $\Delta_{intercept}$, corrected for the effect of laser heating, into
514 the Δ–ρ relation yields a value of 0.707 ± 0.005 g/cm^3, which is consistent with the true
515 value (0.704 g/cm^3) within the error (Table 2).
516 In light of the points raised above, one must ascertain whether correlation exists
517 between the Δ value and laser power in the laser power region bracketing the laser power
518 to be used for the measurement when measuring a sample for which the effect of laser
519 heating on Δ is unknown. If a significant positive value of $|(\partial\Delta/\partial P_{ill})_\rho|$ is obtained, as
520 observed in the natural fluid inclusions of this study, then that value indicates that Δ is
521 reduced by the laser heating and indicates that the density is somewhat underestimated
522 if not corrected for that effect. However, if $|(\partial\Delta/\partial P_{ill})_\rho|$ is not significantly positive, as
523 observed for HPOC in this study and for colorless quartz in earlier studies[48], then one
524 can infer that the effect of laser heating is negligible, at least in that laser power region.
525 If the effect of laser heating is found to be present, then the correction method described

526 in the paragraph above is useful to estimate the density more accurately, whether or not
527 a correction is applied depends on the quality of the data desired by the researchers.
528 However, at least when comparing and interpreting Δ obtained from different mineral
529 species, the presence or absence of laser heating effects should be noted. If laser heating
530 effects on the measurements are not negligible, then we recommend some report of how
531 the ideal measurement conditions were reached and what corrections were made to the
532 raw data to interpret them.
533

534 **5. CONCLUSIONS**

535 Raman spectra of CO_2 were measured at 23–200°C and 7.2–248.7 MPa using a
536 high-pressure optical cell. Fermi diad splits (Δ) decreased concomitantly with increasing
537 temperature at constant density. In addition, the $|(\partial\Delta/\partial T)_\rho|$ is maximum at approx. 0.7
538 g/cm^3; it decreases as the density increases from approx. 0.7 g/cm^3. In combination with
539 the results of the earlier study, we conclude that $|(\partial\Delta/\partial T)_\rho|$ increases gradually from 0.0
540 g/cm^3 to 0.6–0.7g/cm^3; it then decreases as the density increases to 1.2 g/cm^3. Therefore,
541 if the inclusion temperature is increased by a certain temperature by laser heating, the
542 largest decrease in Δ will be observed for inclusions with density of 0.6–0.7 g/cm^3. In

543 contrast, fluid inclusions with very high densities of 1.1–1.2 g/cm^3 are less affected by
544 laser heating.

545 To confirm that the density dependence of $|(\partial\Delta/\partial T)_\rho|$ predicted by HPOC
546 experiments is also valid for natural fluid inclusions, we measured Δ for fluid inclusions
547 with densities ranging from approx. 0.3–1.2 g/cm^3 in Cr-spinel and orthopyroxene at
548 varying laser powers (P_{ill}). We found that, above 0.7 g/cm^3, $|(\partial\Delta/\partial P_{ill})_\rho|$ decreased
549 concomitantly with increasing density. Below 0.7 g/cm^3, it decreased concomitantly
550 with decreasing density. Furthermore, even though $|(\partial\Delta/\partial P_{ill})_\rho|$ become smaller at lower
551 densities below 0.6–0.7g/cm^3, the relative underestimation of density because of laser
552 heating might be rather more severe than for inclusions at 0.6–0.7 g/cm^3. The key
553 finding is that for host minerals with large absorption coefficients at the excitation laser
554 wavelength, laser heating can underestimate the CO_2 density by more than 10%, even
555 at typical laser powers used for inclusion analysis. If the decrease in Δ because of laser
556 heating is not negligible, then a more accurate fluid density is obtainable by estimating
557 the intercept Δ ($\Delta_{intercept}$, i.e. Δ at 0 mW) from the correlation between Δ and laser power,
558 and substituting it into the Δ–ρ relation.

559

560 **ACKNOWLEDGMENTS**

We would like to thank Marie-Camille Caumon and an anonymous reviewer for constructive reviews that greatly improved this manuscript. We are grateful to Robert J. Bodnar and Eszter Sendula for their comments related to the original draft of this manuscript. This study was supported by Grants-in-Aid for Scientific Research (Nos. 23654160, 25287139, 26610136, 16H04079, 16J0472207, and 19J21537) from the Japan Society for the Promotion of Science.

REFERENCES

[1] E. Roedder, *Fluid inclusions. Reviews in Mineralogy*, **1984**, vol. 12.

[2] R. J. Bodnar, P. Lecumberri-Sanchez, D. Moncada, M. Steele-MacInnis, *Fluid Inclusions in Hydrothermal Ore Deposits*, Elsevier Ltd., 2nd edn., **2014**, vol. 13.

[3] E. L. Klein, K. Fuzikawa, *Ore Geol. Rev.* **2010**, *37*, 31.

[4] R. C. Newton, J. V. Smith, B. F. Windley, *Nature* **1980**, *288*, 45.

[5] W. M. Lamb, J. W. Valley, P. E. Brown, *Contrib. to Mineral. Petrol.* **1987**, *96*, 485.

[6] H. M. Lamadrid, W. M. Lamb, M. Santosh, R. J. Bodnar, *Gondwana Res.* **2014**, *26*, 301.

[7] J. L. R. Touret, *Lithos* **2001**, *55*, 1.

[8] M. L. Frezzotti, S. Ferrando, F. Tecce, D. Castelli, *Earth Planet. Sci. Lett.* **2012**, *351–352*, 70.

[9] T. Andersen, E.-R. Neumann, *Lithos* **2001**, *55*, 301.

[10] E. Oglialoro, M. L. Frezzotti, S. Ferrando, C. Tiraboschi, C. Principe, G. Groppelli, I. M. Villa, *Bull. Volcanol.* **2017**, *79*, 70.

[11] G. Levresse, K. E. C. la Cruz, J. JorgeAranda-Gómez, M. GuadalupeDávalos-Elizondo, S. Jiménez-Sandoval, F. Rodríguez-Melgarejo, L. A. Alba-Aldave, *J.*

586 *Volcanol. Geotherm. Res.* **2016**, *310*, 72.

587 [12] T. H. Hansteen, A. Klügel, H. U. Schmincke, *Contrib. to Mineral. Petrol.* **1998**,
588 *132*, 48.

589 [13] V. Zanon, M. L. Frezzotti, *Geochemistry, Geophys. Geosystems* **2013**, *14*, 3494.

590 [14] J. Yamamoto, H. Kagi, Y. Kawakami, N. Hirano, M. Nakamura, *Earth Planet.*
591 *Sci. Lett.* **2007**, *253*, 369.

592 [15] J. Yamamoto, K. Nishimura, H. Ishibashi, H. Kagi, S. Arai, V. S. Prikhod'ko,
593 *Tectonophysics* **2012**, *554–557*, 74.

594 [16] J. Yamamoto, J. Korenaga, N. Hirano, H. Kagi, *Geology* **2014**, *42*, 967.

595 [17] E. Bali, Z. Zajacz, I. Kovács, C. Szabó, W. Halter, O. Vaselli, K. Török, R. J.
596 Bodnar, *J. Petrol.* **2008**, *49*, 421.

597 [18] J. Yamamoto, H. Kagi, I. Kaneoka, Y. Lai, V. S. Prikhod'ko, S. Arai, *Earth*
598 *Planet. Sci. Lett.* **2002**, *198*, 511.

599 [19] L. R. Moore, E. Gazel, R. Tuohy, A. S. Lloyd, R. Esposito, M. Steele-MacInnis,
600 E. H. Hauri, P. J. Wallace, T. Plank, R. J. Bodnar, *Am. Mineral.* **2015**, *100*, 806.

601 [20] T. Hanyu, J. Yamamoto, K. Kimoto, K. Shimizu, T. Ushikubo, *Chem. Geol.*
602 **2020**, *557*, 119855.

603 [21] P. Robidoux, M. L. Frezzotti, E. H. Hauri, A. Aiuppa, *J. Petrol.* **2018**, *59*, 2093.

604 [22] S. Venugopal, F. Schiavi, S. Moune, N. Bolfan-casanova, T. Druitt, G. Williams-
605 jones, *Sci. Rep.* **2020**, *10*, 9034.

606 [23] C. M. Allison, K. Roggensack, A. B. Clarke, *Nat. Commun.* **2021**, *12*, 217.

607 [24] N. L. Mironov, D. P. Tobelko, S. Z. Smirnov, M. V. Portnyagin, S. P.
608 Krasheninnikov, *Russ. Geol. Geophys.* **2020**, *61*, 600.

609 [25] K. M. Rosso, R. J. Bodnar, *Geochim. Cosmochim. Acta* **1995**, *59*, 3961.

610 [26] T. Kobayashi, J. Yamamoto, T. Hirajima, H. Ishibashi, N. Hirano, Y. Lai, V. S.
611 Prikhod'Ko, S. Arai, *J. Raman Spectrosc.* **2012**, *43*, 1126.

612 [27] H. M. Lamadrid, L. R. Moore, D. Moncada, J. D. Rimstidt, R. C. Burruss, R. J.
613 Bodnar, *Chem. Geol.* **2017**, *450*, 210.

614 [28] X. Wang, I. M. Chou, W. Hu, R. C. Burruss, Q. Sun, Y. Song, *Geochim.*
615 *Cosmochim. Acta* **2011**, *75*, 4080.

[29] J. Yamamoto, H. Kagi, *Chem. Lett.* **2006**, *35*, 610.

[30] Y. Song, I. Chou, W. Hu, R. Burruss, W. Lu, *Acta Geol. Sin.* **2009**, *83*, 932.

[31] A. Fall, B. Tattitch, R. J. Bodnar, *Geochim. Cosmochim. Acta* **2011**, *75*, 951.

[32] X. Yuan, R. A. Mayanovic, H. Zheng, Q. Sun, *Am. Mineral.* **2017**, *102*, 404.

[33] V. H. Le, M. C. Caumon, A. Tarantola, A. Randi, P. Robert, J. Mullis, *Anal. Chem.* **2019**, *91*, 14359−14367.

[34] V. H. Le, M. C. Caumon, A. Tarantola, A. Randi, P. Robert, J. Mullis, *Chem. Geol.* **2020**, *552*, 119783.

[35] W. Wang, M. C. Caumon, A. Tarantola, J. Pironon, W. Lu, Y. Huang, *Chem. Geol.* **2019**, *528*, 119281.

[36] D. M. Sublett, E. Sendula, H. Lamadrid, M. Steele-MacInnis, G. Spiekermann, R. C. Burruss, R. J. Bodnar, *J. Raman Spectrosc.* **2020**, *51*, 555.

[37] Y. Hagiwara, J. Torimoto, J. Yamamoto, *J. Raman Spectrosc.* **2020**, *51*, 1003.

[38] J. F. Bertrán, *Spectrochim. Acta Part A Mol. Spectrosc.* **1983**, *39*, 119.

[39] Y. Garrabos, V. Chandrasekharan, M. A. Echargui, F. Marsault-Herail, *Chem. Phys. Lett.* **1989**, *160*, 250.

[40] C. H. Wang, R. B. Wright, *Chem. Phys. Lett.* **1973**, *23*, 241.

[41] R. B. Wright, C. H. Wang, *J. Chem. Phys.* **1973**, *58*, 2893.

[42] Y. Kawakami, J. Yamamoto, H. Kagi, *Appl. Spectrosc.* **2003**, *57*, 1333.

[43] D. M. Sublett, E. Sendula, H. M. Lamadrid, M. Steele-MacInnis, G. Spiekermann, R. J. Bodnar, *J. Raman Spectrosc.* **2020**, *52*, 750.

[44] J. Chen, H. Zheng, W. Xiao, Y. Zeng, K. Weng, *Geochim. Cosmochim. Acta* **2004**, *68*, 1355.

[45] J. C. Seitz, J. D. Pasteris, I.-M. Chou, *Am. J. Sci.*, **1996**, 296, 577–600.

[46] H. M. Lamadrid, M. Steele-MacInnis, R. J. Bodnar, *J. Raman Spectrosc.* **2018**, *49*, 581.

[47] S. Remigi, T. Mancini, S. Ferrando, M. L. Frezzotti, *Appl. Spectrosc.* (in press)

[48] Y. Hagiwara, K. Yoshida, A. Yoneda, J. Torimoto, J. Yamamoto, *Chem. Geol.* **2021**, *559*, 119928.

[49] A. Hacura, *Phys. Lett. A* **1997**, *227*, 237.

[50] G. V. Bondarenko, *J. Appl. Spectrosc.* **1986**, *45*, 1285.

[51] K. S. Pitzer, S. M. Sterner, *J. Chem. Phys.* **1994**, *101*, 3111.

[52] S. Fukura, T. Mizukami, S. Odake, H. Kagi, *Appl. Spectrosc.* **2006**, *60*, 946.

[53] E. S. Izraeli, J. W. Harris, O. Navon, *Earth Planet. Sci. Lett.* **1999**, *173*, 351.

[54] R. G. Dickinson, R. T. Dillon, F. Rasetti, *Phys. Rev.* **1929**, *34*, 582.

[55] G. Herzberg, *Infrared and Raman Spectra of Polyatomic Molecules, Molecular Spectra and Molecular Structure II*, **1945**.

[56] M. Arakawa, J. Yamamoto, H. Kagi, *Chem. Lett.* **2008**, *37*, 280.

[57] M. S. Brown, R. R. Steeper, *Appl. Spectrosc.* **1991**, *45*, 1733.

[58] Y. Hagiwara, K. Takahata, J. Torimoto, J. Yamamoto, *J. Raman Spectrosc.* **2018**, *49*, 1776.

[59] M. Berkesi, K. Hidas, T. Guzmics, J. Dubessy, R. J. Bodnar, C. Szabo, B. Vajna, T. Tsunogae, *J. Raman Spectrosc.* **2009**, *40*, 1461.

[60] R. Span, W. Wagner, *J. Phys. Chem. Ref. Data*, **1996**, 25, 1509–1596.

[61] M. N. Taran, F. Parisi, D. Lenaz, A. A. Vishnevskyy, *Phys. Chem. Miner.* **2014**, *41*, 593.

[62] M. N. Taran, K. Langer, *Phys. Chem. Miner.* **2001**, *28*, 199.

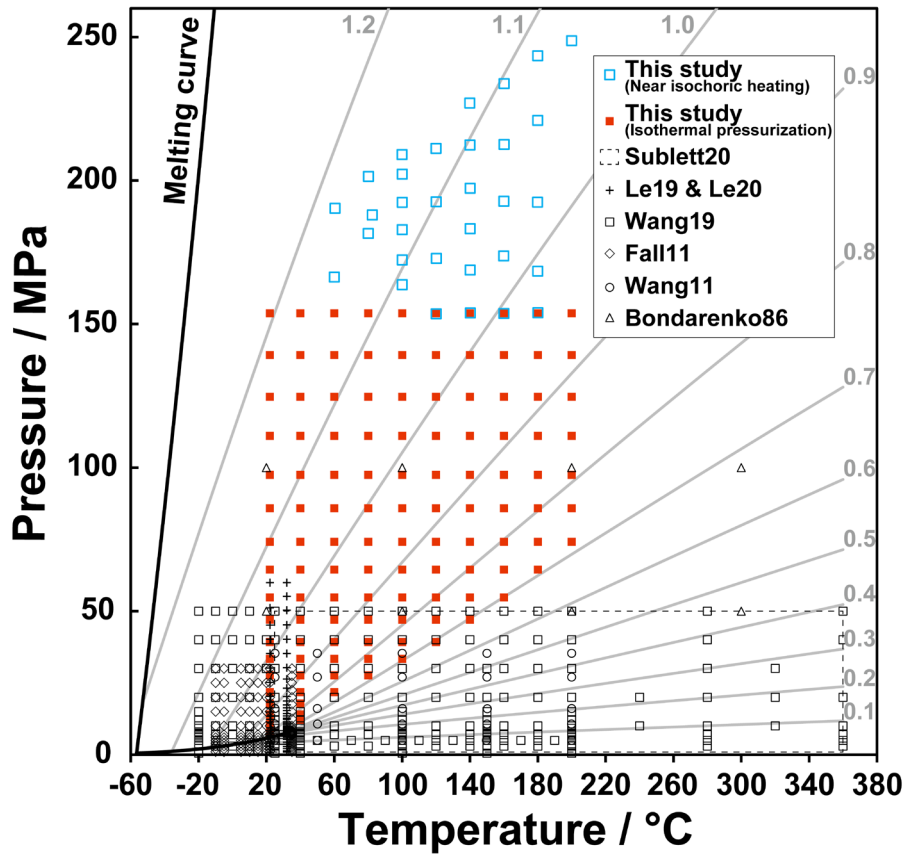

Figure 1 *P–T* projection of the CO_2 phase diagram showing locations of all data measured for this study. Filled red squares show *P–T* conditions at which measurements are made using isothermal pressurization experiments. Open blue squares denote *P–T* conditions at which measurements are made using near isochoric heating experiments. The black symbols give *P–T* conditions under which measurements were made in earlier studies using a high-pressure optical cell and fused silica capillary capsule.[28,31,33,34,43,50] Black solid lines are phase coexistence curves. Grey ones are isochore calculated using Pitzer and Sterner[51] EOS. Contours are labeled according to fluid density (g/cm^3). The data shown are those presented in Tables S1 and S2.

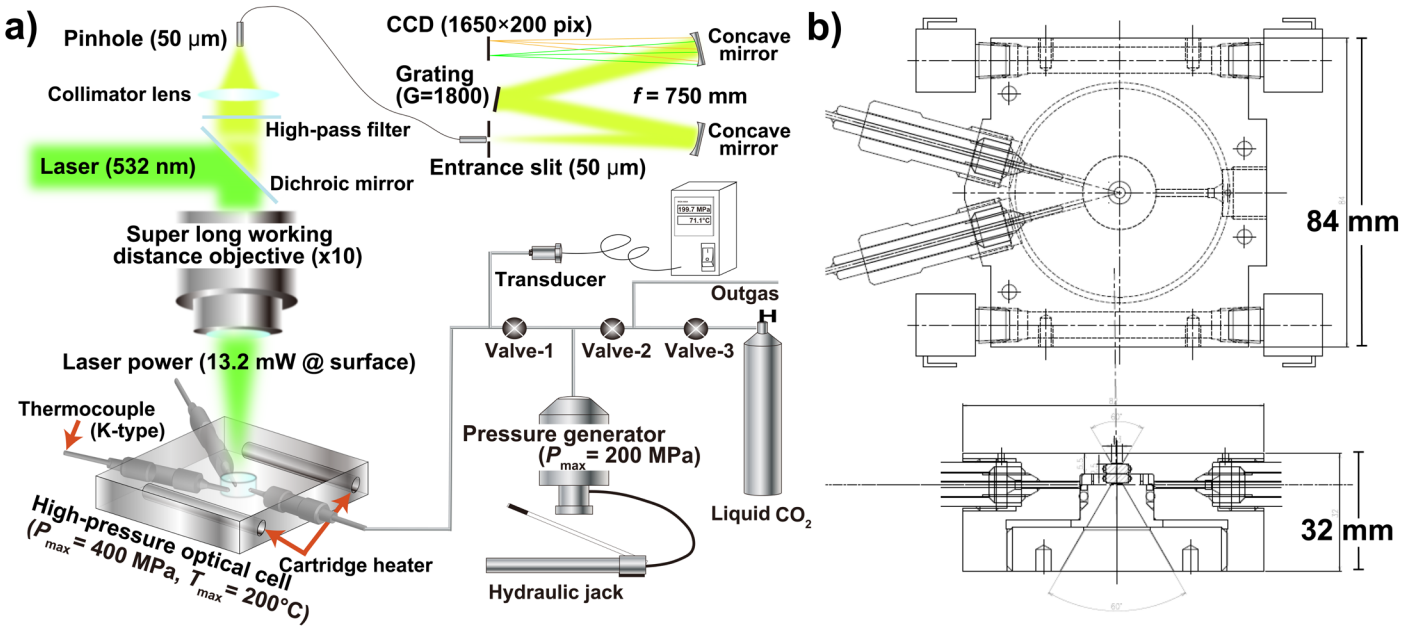

Figure 2 (a) Schematic diagram of experimental apparatus used for high-*P*–*T* Raman spectroscopic investigation. CO_2 is loaded into the HPOC from the right side through stainless steel tubing with outer diameter of 1/16 inch. During the near isochoric heating experiments, the fluid pressure in the cell was adjusted by gradually loosening valve-1. The excitation laser (532 nm) was focused on the CO_2 fluid through a 10× objective lens. The laser power was 13.2 mW at the surface of optical window. (b) Cross-sections of the HPOC. It is equipped with a 2.5-mm-thick sapphire optical window that is transparent to visible light.

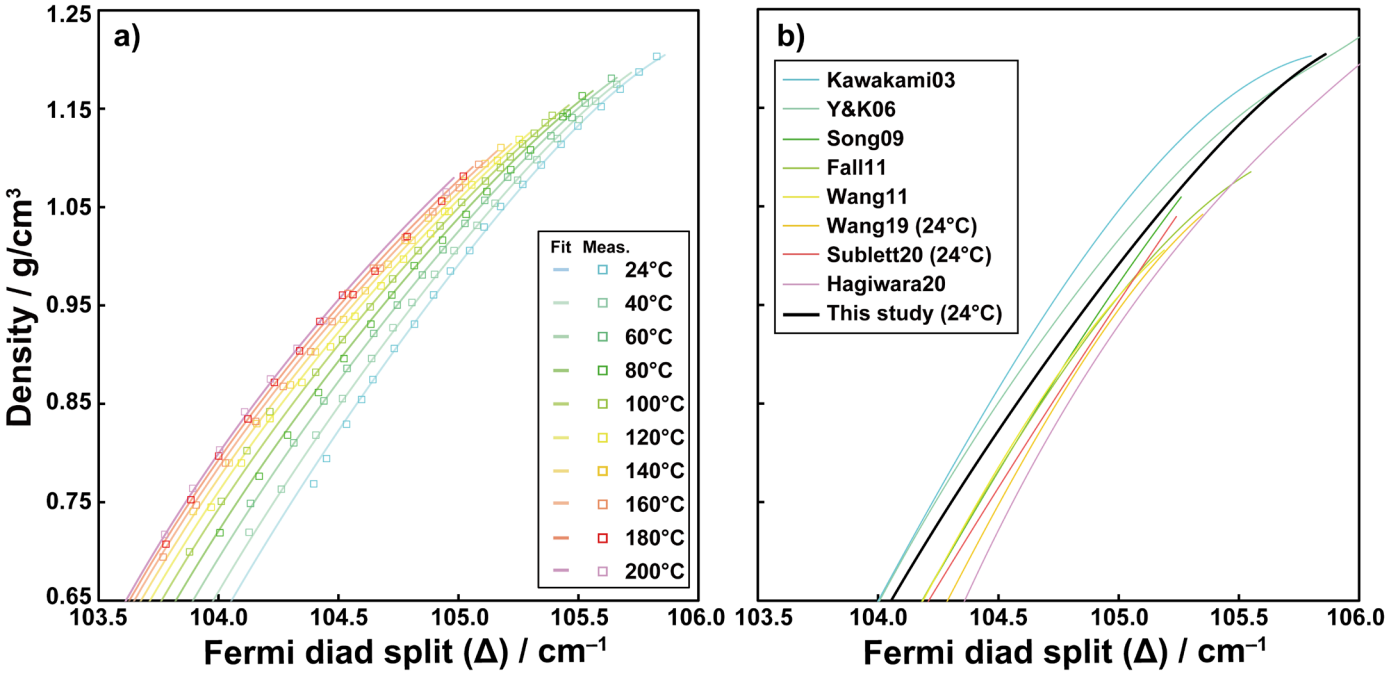

Figure 3 (a) Relation of CO_2 density and Fermi diad (Δ) as a function of temperature. Raman spectra of CO_2 are measured at temperatures of 23–200°C and pressures of 7.2–248.7 MPa using HPOC. For this study, the density corresponding to the temperature and pressure condition of every analysis was calculated according to Span and Wagner[60] EOS for CO_2. The data shown are those from Tables S1 and S2. **(**b) Comparison of published Δ–ρ relations. All densimeters shown are within the density region in which calibration measurements were made and effective at near room temperature.[28–31,35,37,42,43]

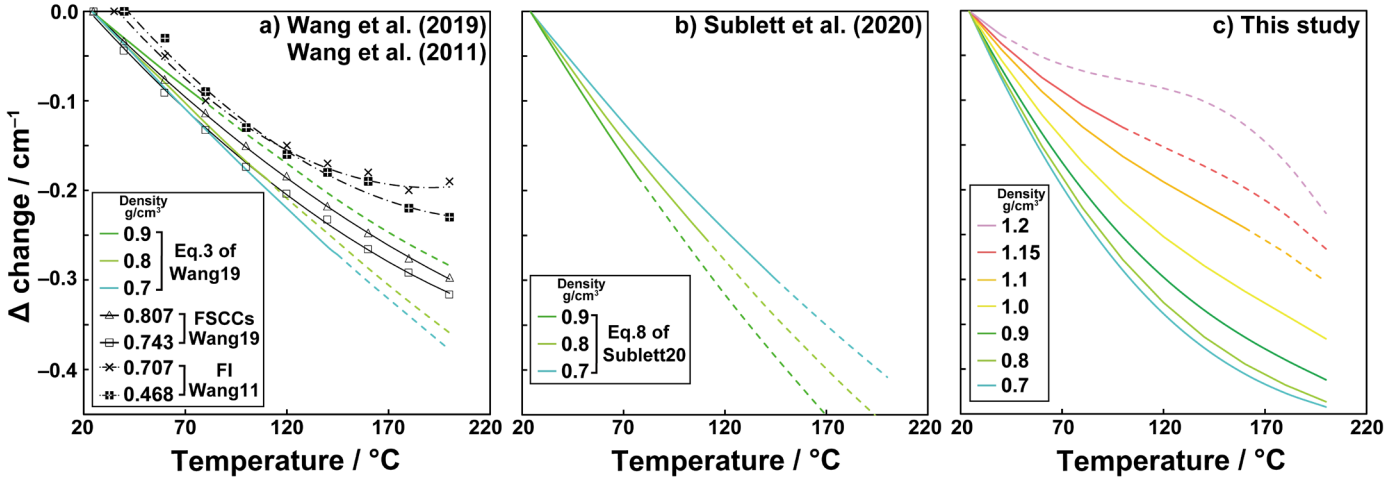

Figure 4 Δ change relative to initial Δ obtained at approx. 24°C as a function of temperature. Colored solid lines show the temperature dependence of Δ at constant density calculated using (a) Equation (3) of Wang et al.[35], (b) Equation (8) of Sublett et al.[43], and (c) Equation (2) of this study. The dotted line shows the extrapolation of the Δ–*T*–*ρ* relation derived in each study to the *P*–*T* region where no experimental calibration has been performed. (a, b) Colored solid lines are isochores at 0.7, 0.8, and 0.9 g/cm^3. (a) Black solid lines with open symbols are data obtained from the FSCCs with densities of 0.807 and 0.743 g/cm^3 by Wang et al.[35]. Dashed–dotted lines show data obtained from the fluid inclusions with densities of 0.707 and 0.468 g/cm^3 by Wang et al.[28]. (c) Colored solid lines are isochores at 0.7, 0.8, 0.9, 1.0, 1.1, 1.15, and 1.2 g/cm^3.

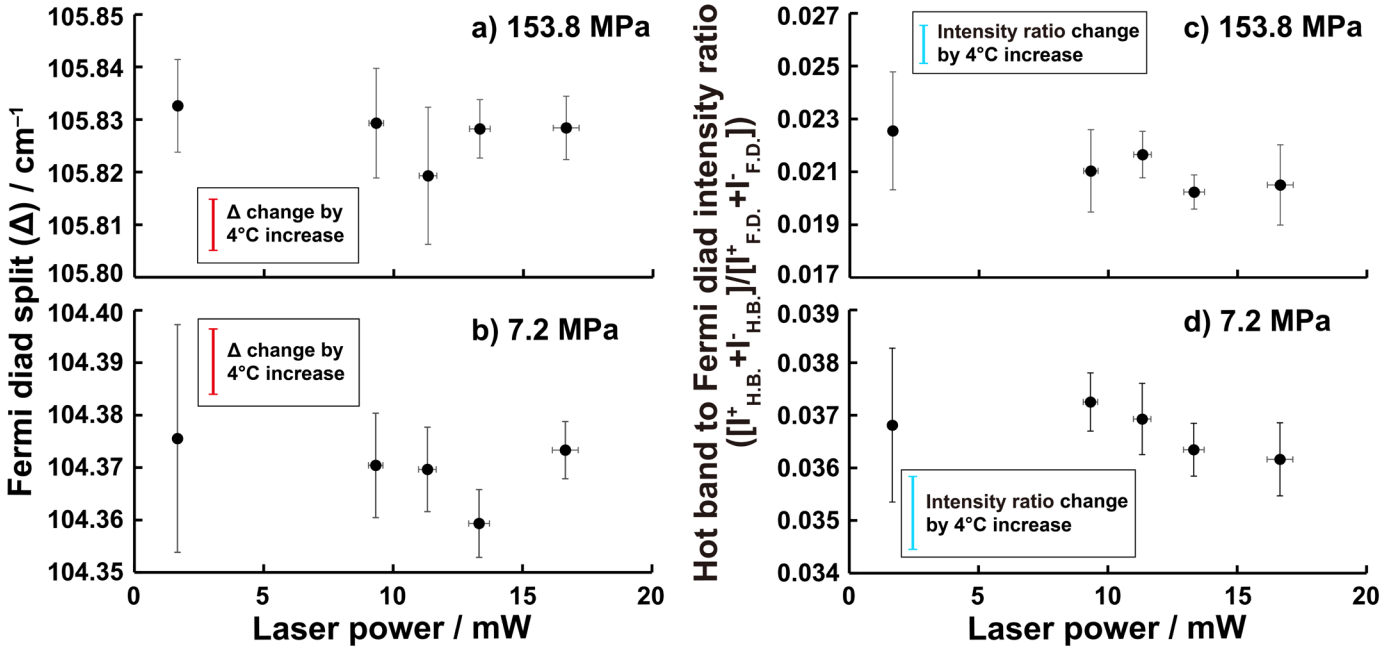

Figure 5 Fermi diad split (Δ) (a, b) and hot band to the Fermi diad intensity ratio (c, d) of CO_2 with pressures of 153.8 MPa (a, c) and 7.2 MPa (b, d) as a function of the laser power at the sapphire window surface. Red bars represent the expected Δ change attributable to the temperature change of 4°C under measured *P*–*T* conditions calculated using Equation (2). The blue bar represents the expected $\left[I^{+}_{\mathrm{H.B.}}+I_{\mathrm{H.B.}}\right]/\left[I^{+}_{\mathrm{F.D.}}+I_{\mathrm{F.D.}}\right]$ change attributable to temperature change of 4°C under measured *P*–*T* conditions calculated using Equation (5) of Hagiwara et al.[48]. Measurements were made five times at each laser power. Error bars represent 1σ. Data shown are from Table 1.

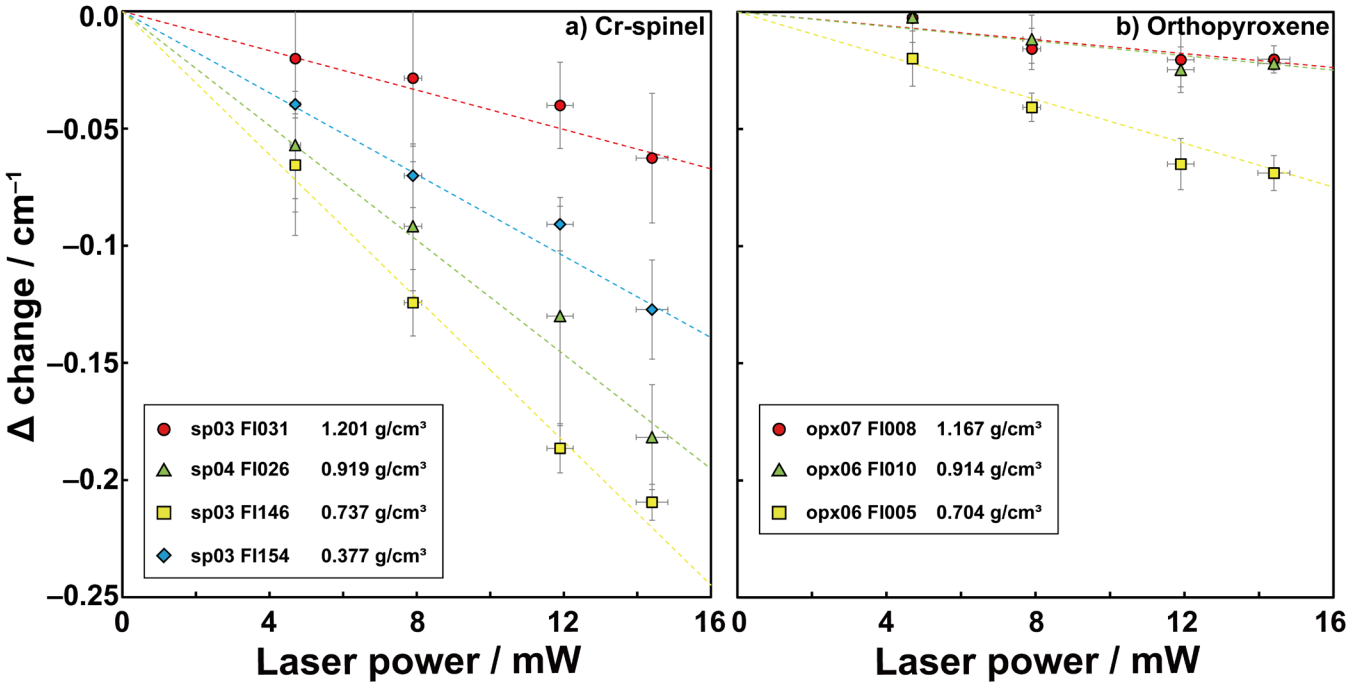

Figure 6 Δ change of CO_2-rich fluid inclusions hosted in Cr-spinel and orthopyroxene versus laser power. The vertical axis shows deviation of the measured Δ (Δ_{calib}) from the Δ value at 0 mW ($\Delta_{intercept}$) estimated from the intercept of the linear fit of the measured Δ and laser power. Error bars for Δ show the standard deviation (n = 5). Those for laser power are 3%. Dashed lines show linear fit (York method) to four data points. (a) Red, green, yellow, and blue symbols respectively represent fluid inclusions with densities of 1.201, 0.919, 0.737, and 0.377 g/cm^3 in Cr-spinel. (b) Red, green and yellow symbols respectively represent fluid inclusions with densities of 1.167, 0.914, and 0.704 g/cm^3 in orthopyroxene.

Table 1 Variation of hot bands to the Fermi diad intensity ratio and Δ of CO_2 in HPOC at 153.8 and 7.2 MPa at different laser powers.

ρ [a]	T	P	P_{ill}	$\Delta_{Ne\ calib}$ [b]	Error [c]	HBR [d]	Error [c]
g/cm^3	°C	MPa	mW	cm^{-1}	cm^{-1}		
1.204	23.0	153.8	1.7	105.833	0.009	0.0226	0.0022
1.204	23.0	153.8	9.3	105.829	0.010	0.0210	0.0016
1.204	22.9	153.8	11.3	105.819	0.013	0.0217	0.0009
1.204	23.0	153.8	13.3	105.828	0.006	0.0202	0.0006
1.204	23.0	153.8	16.7	105.828	0.006	0.0205	0.0015
0.783	22.7	7.2	1.7	104.376	0.022	0.0368	0.0015
0.784	22.6	7.2	9.3	104.370	0.010	0.0373	0.0006
0.783	22.7	7.2	11.3	104.370	0.008	0.0369	0.0007
0.783	22.7	7.2	13.3	104.359	0.006	0.0363	0.0005
0.783	22.7	7.2	16.7	104.373	0.005	0.0362	0.0007

[a] Densities calculated according to Span and Wagner[60] EOS.

[b] Calculated from Equation (1).

[c] Error is standard deviation (n = 5).

[d] HBR: Hot bands to the Fermi diad intensity ratio.

Table 2 Relation between Δ_{calib} and P_{ill} obtained from natural fluid inclusions with various densities, and the density corrected for the effect of laser heating ($\rho_{\Delta_{intercept}}$) as estimated from the relation.

Sample name	ρ_{T_h} [a]	$\rho_{\Delta_{intercept}}$ [b]	$\rho_{\Delta_{calib}}$ [c]	P_{ill}	$\sigma_{P_{ill}}$	Δ_{calib}	σ_{Δ} [e]	$\Delta_{intercept}$	Error [f]	$(\partial\Delta/\partial P_{ill})_{\rho}$	Error [f]
	g/cm^3	g/cm^3	g/cm^3	mW	mW	cm^{-1}	cm^{-1}	cm^{-1}	cm^{-1}	cm^{-1}/mW	cm^{-1}/mW
spinel03 fi031	n.d.	1.201	1.198	4.7	0.14	105.827	0.024	105.848	0.035	–0.0038	0.0033
			1.197	7.9	0.24	105.819	0.029				
			1.195	11.9	0.36	105.807	0.018				
			1.191	14.4	0.43	105.785	0.028				
spinel04 fi026	n.d.	0.919	0.897	4.7	0.14	104.730	0.023	104.793	0.033	–0.0127	0.0032
			0.885	7.9	0.24	104.696	0.027				
			0.871	11.9	0.36	104.657	0.047				
			0.853	14.4	0.43	104.606	0.022				
spinel03 fi146	n.d.	0.737	0.714	4.7	0.14	104.232	0.020	104.290	0.024	–0.0143	0.0020
			0.690	7.9	0.24	104.173	0.014				
			0.665	11.9	0.36	104.111	0.010				
			0.655	14.4	0.43	104.088	0.008				
spinel03 fi154	n.d.	0.377 [d]	0.363	4.7	0.14	103.360 [d]	0.056	103.393 [d]	0.036	–0.0075	0.0033
			0.350	7.9	0.24	103.330 [d]	0.013				
			0.341	11.9	0.36	103.309 [d]	0.011				
			0.325	14.4	0.43	103.273 [d]	0.021				
opx07 fi008	1.167	1.170	1.169	4.7	0.14	105.672	0.011	105.675	0.013	–0.0015	0.0011
			1.166	7.9	0.24	105.659	0.009				
			1.165	11.9	0.36	105.655	0.012				
			1.165	14.4	0.43	105.655	0.006				
opx06 fi010	0.914	0.898	0.896	4.7	0.14	104.728	0.020	104.730	0.018	–0.0016	0.0013
			0.893	7.9	0.24	104.719	0.010				
			0.888	11.9	0.36	104.706	0.010				
			0.889	14.4	0.43	104.708	0.003				

opx06 fi005	0.704	0.707	0.699	4.7	0.14	104.195	0.012	104.215	0.013	–0.0047	0.0012
			0.692	7.9	0.24	104.178	0.006				
			0.682	11.9	0.36	104.154	0.011				
			0.681	14.4	0.43	104.150	0.007				

[a] Densities calculated using Span and Wagner[60] EOS from measured partial homogenization temperatures of the carbonate phase to liquid; +25.4°C for opx06 fi005, +2.2°C for opx06 fi010, and –53.4°C for opx07 fi008. n.d.: not determined.

[b] $\rho_{\Delta_{intercept}}$ was obtained by substituting $\Delta_{intercept}$ and 20°C into Equation (2).

[c] $\rho_{\Delta_{calib}}$ was obtained by substituting Δ_{calib} and 20°C into Equation (2).

[d] Density for this sample is obtained by substituting $\Delta_{intercept}$ into Equation of Kawakami et al.[42] because the experimental calibration of Equation (2) of this study did not cover density lower than approx. 0.7 g/cm^3.

[e] Error is standard deviation (n = 5).

[f] Error is standard error.

Table 3 Fitting coefficients of Equation (2).

	Value	Std. Error
a	−61821.3575	22680.0066
b	-3.3585×10^{-4}	3.9008×10^{-5}
c	1.56567×10^{-8}	3.5554×10^{-9}
d	1781.1957586	655.5483091
e	−17.112171653	6.316553270
f	0.0548181541	0.0202894536
g	0.00119219	8.247×10^{-5}
h	−0.0000112203	7.8256×10^{-7}
i	3.12805×10^{-6}	3.672×10^{-7}
j	-1.02847×10^{-46}	3.6190×10^{-47}